

Observation of quantum phase synchronization in a nuclear-spin systemV. R. Krithika,^{1,*} Parvinder Solanki^{2,†} Sai Vinjanampathy,^{2,3,‡} and T. S. Mahesh^{1,§}¹*Department of Physics and NMR Research Center, Indian Institute of Science Education and Research, Pune 411008, India*²*Department of Physics, Indian Institute of Technology Bombay, Powai, Mumbai 400076, India*³*Centre for Quantum Technologies, National University of Singapore, 3 Science Drive 2, 117543 Singapore, Singapore*

(Received 28 December 2021; accepted 19 May 2022; published 7 June 2022)

We report an experimental study of phase synchronization in a pair of interacting nuclear spins subjected to an external drive in nuclear magnetic resonance architecture. A weak transition-selective radio-frequency field applied on one of the spins is observed to cause phase localization, which is experimentally established by measuring the Husimi distribution function under various drive conditions. To this end, we have developed a general interferometric technique to directly extract values of the Husimi function via the transverse magnetization of the undriven nuclear spin. We further verify the robustness of synchronization to detuning in the system by studying the Arnold tongue behavior.

DOI: [10.1103/PhysRevA.105.062206](https://doi.org/10.1103/PhysRevA.105.062206)**I. INTRODUCTION**

Motivated by the stability and ubiquity of classical synchronization [1], quantum synchronization has been a field of intense study. Platforms that exhibit quantized dynamics have inspired theoretical studies in systems such as trapped ions [2,3], superconducting circuits [4], atomic ensembles [5], optomechanical systems [6–9], and nanomechanical systems [10,11]. Theoretical studies have shown fundamental implications of synchronization to other fields such as entanglement generation [12,13], thermodynamics [14,15], quantum networks [16], and continuous-time crystals [17].

Following the definition of classical synchronization [1], quantum synchronization can be understood as the adjustment of rhythms of quantum limit cycle oscillators under the effect of weak coupling or an external drive [13,15,18,19]. For detailed discussion on other existing definitions of quantum synchronization, we refer to [15]. Quantum synchronization proceeds by first considering the quantum analog of phase space, which is one of many quasiprobability distributions such as the Husimi function and Wigner function [20]. A valid limit cycle requires robustness against external perturbations and a neutral free phase [1]. Thermal states were shown to be examples of such limit cycle states, showing an equiprobable distribution of phases in phase space [14]. Such phase-space distribution functions have been used to construct measures of synchronization [7,21–24]. Following several studies of synchronization in specific systems, unified measures of quantum synchronization based on relative entropies have also been formulated [19]. They used information-theoretic measures based on quantum correlations, which have been shown to

measure synchronization [13,25,26]. These measures reduce to the phase-space-based measures under the system-specific conditions [19].

Following this theoretical interest [7,8,13–15,18,19,27–33], quantum synchronization has been experimentally demonstrated recently in the IBM quantum computer [34] and spin-1 cold atoms [35]. The experimental demonstration of quantum synchronization is in general a challenging task owing to the difficulty in extracting required parameters. Quantum synchronization measurements typically require the system to settle into a steady state, which necessitates the need for long waiting times. Such long wait times allow for other experimental noise sources to interfere with the signal. Besides this, tomographic reconstruction of the state scales with the system size, requiring $O(n^2)$ measurements for a system of dimension n [36]. Thus, the steady-state characteristics of the system are inferred by extrapolating transient dynamics or by devising complicated measurement schemes.

Here we resolve the aforementioned issues and report the observation of synchronization in nuclear spins. Nuclear magnetic resonance (NMR) architecture allows convenient control and manipulation of multispin systems using radio-frequency (rf) pulses. These, in addition to inherent relaxation mechanisms, which cause the system to thermalize, offer an ideal platform to observe synchronization. Our experiment involves a pair of interacting spin-1/2 nuclei and a weak transition-selective rf field applied on one of the spins. The resulting phase localization is characterized using Husimi distribution, which typically needs quantum state tomography (QST) [37]. However, QST after a long external drive proved to be highly inefficient because, as the steady state is approached, the irradiated levels saturate and relevant transitions become too faint. We overcome this by introducing an interferometric technique that can experimentally capture the Husimi Q function directly. In addition, this method can be adapted beyond synchronization to other studies that rely on coherence measurements, even weak ones. By measuring the NMR system

*krithika_vr@students.iiserpune.ac.in

†psolanki@phy.iitb.ac.in

‡sai@phy.iitb.ac.in

§mahesh.ts@iiserpune.ac.in

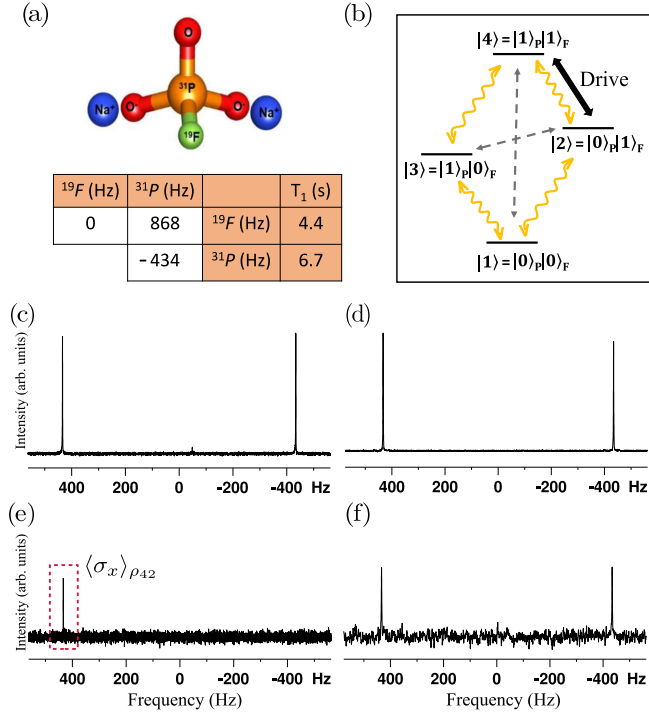


FIG. 1. (a) Sodium fluorophosphate molecular structure with its Hamiltonian parameters and the spin-lattice relaxation time constants T_1 shown in the table. The diagonal elements represent the offset, while off-diagonal element represents the scalar J coupling constant. (b) Energy levels of the two-qubit system with four nondegenerate energy eigenstates. The numerical model presented here considers only the single-quantum relaxation pathways (yellow curved arrows) and ignores the zero- and double-quantum pathways (dashed gray arrows). Also shown are reference NMR spectra of (c) ^{31}P and (d) ^{19}F spins, each obtained with a 90° pulse on the thermal equilibrium state, and (e) the ^{31}P NMR signal after a 100 s drive on the $|2\rangle \leftrightarrow |4\rangle$ transition. The intensity of the ρ_{42} element is indicated in the dashed box, which is used for the Arnold tongue analysis. (f) The ^{19}F NMR spectrum at the end of the interferometric circuit from which we can directly extract the Husimi distribution at particular θ and ϕ values.

in the process of reaching the steady state, we investigate transient as well as steady-state behavior of the system under the influence of the external drive. We also explore the robustness of synchronization against detuning frequency and drive strength via the Arnold tongue.

This article is organized as follows. In Sec. II we introduce the spin system and outline the theory as well as measures of quantum synchronization. In Sec. III we explain the NMR architecture, the experimental setup, and the numerical model. The interferometric measurement of the Husimi distribution (IMHD) is described in Sec. IV. Following this, we discuss the corresponding experimental results in Sec. V. We summarize in Sec. VI.

II. SYNCHRONIZATION OF A FOUR-LEVEL SYSTEM

We consider a nondegenerate four-level system composed of ^{19}F and ^{31}P nuclei in sodium fluorophosphate molecule, as shown in Figs. 1(a) and 1(b), and study the phase synchroniza-

tion of the system with an external drive. The extent of phase localization of the system in a state ρ can be quantified using the Husimi-Kano Q representation function [38,39]. For the given four-level system it can be defined as

$$Q(\theta_1, \theta_2, \theta_3, \phi_1, \phi_2, \phi_3) = \frac{24}{\pi^3} \langle \hat{n}_4 | \rho | \hat{n}_4 \rangle, \quad (1)$$

where

$$|\hat{n}_4\rangle = (C_{\theta_1}, e^{i\phi_1} S_{\theta_1} C_{\theta_2}, e^{i\phi_2} S_{\theta_1} S_{\theta_2} C_{\theta_3}, e^{i\phi_3} S_{\theta_1} S_{\theta_2} S_{\theta_3})^T$$

is the SU(4) coherent state [40–42] with $C_{\theta_i} = \cos(\theta_i/2)$ and $S_{\theta_i} = \sin(\theta_i/2)$. A brief review of spin coherent states is presented in Appendix A. The normalization of the Q function arises from the completeness relation of coherent state $|\hat{n}_4\rangle$ defined as

$$\int |\hat{n}_4\rangle \langle \hat{n}_4| d\mu = \frac{\pi^3}{24} \mathbb{1}, \quad (2)$$

where the integration is taken over the Haar measure and volume element given by [41]

$$d\mu = d\theta_1 d\theta_2 d\theta_3 d\phi_1 d\phi_2 d\phi_3 C_{2\theta_1} S_{2\theta_1}^5 C_{2\theta_2} S_{2\theta_2}^3 C_{2\theta_3} S_{2\theta_3}.$$

For a system with internal Hamiltonian $H_0 = \sum_{i=1}^4 \omega_i |i\rangle \langle i|$ having characteristic frequencies ω_i , the spin coherent state evolves as

$$e^{-iH_0 t} |\hat{n}_4\rangle \rightarrow \begin{pmatrix} C_{\theta_1} \\ e^{i(\phi_1 - \omega_{21}t)} S_{\theta_1} C_{\theta_2} \\ e^{i(\phi_2 - \omega_{31}t)} S_{\theta_1} S_{\theta_2} C_{\theta_3} \\ e^{i(\phi_3 - \omega_{41}t)} S_{\theta_1} S_{\theta_2} S_{\theta_3} \end{pmatrix}, \quad (3)$$

where $\omega_{i1} = \omega_i - \omega_1$. Under the free evolution of the internal Hamiltonian, the ϕ_i represent the free phases oscillating with the respective frequencies ω_{i1} , while the θ_i govern the populations of the system which remains fixed. In the absence of any external perturbation, the steady state reached by the thermalization has a uniform phase distribution and the Husimi Q function remains independent of (ϕ_1, ϕ_2, ϕ_3) . This points to the fact that the given system has free phases available. Along with the existence of free phases, a system needs to be nonlinear in nature to exhibit limit cycle behavior. Since the dynamics of a multilevel quantum system is generally nonlinear, the availability of free phases makes it a perfect candidate to study synchronization. On application of a weak external drive, the system may develop a definite phase relationship with the drive, thus resulting in a localized phase distribution. This phenomenon, known as phase synchronization, is captured and quantified by

$$S(\phi_1, \phi_2, \phi_3) = \int d\Theta Q(\theta_1, \theta_2, \theta_3, \phi_1, \phi_2, \phi_3) - \frac{1}{(2\pi)^3}, \quad (4)$$

where $d\Theta = d\theta_1 d\theta_2 d\theta_3 C_{2\theta_1} S_{2\theta_1}^5 C_{2\theta_2} S_{2\theta_2}^3 C_{2\theta_3} S_{2\theta_3}$. For the four-level system considered here, the expression (4) leads to

$$S(\phi_1, \phi_2, \phi_3) = \frac{1}{16\pi^2} \text{Re}(\rho_{43} e^{i\phi_1} + \rho_{42} e^{i\phi_2} + \rho_{41} e^{i\phi_3} + \rho_{32} e^{i(\phi_2 - \phi_1)} + \rho_{31} e^{i(\phi_3 - \phi_1)} + \rho_{21} e^{i(\phi_3 - \phi_2)}), \quad (5)$$

where $\rho_{ij} = \langle i|\rho|j\rangle$. Under the effect of thermal baths and in the absence of external perturbations or drive, the system reaches its thermal equilibrium state, which is diagonal in the energy eigenbasis of the internal Hamiltonian. The Husimi Q function for a diagonal state reduces to a uniform distribution showing no phase localization. Therefore, the thermal state constitutes a valid limit cycle state which is stable to external perturbation and has free phases [14,19]. Furthermore, the synchronization measure $S(\phi_1, \phi_2, \phi_3)$ registers zero for such a limit cycle state.

System with a drive. Let us now study the entrainment of the given limit cycle oscillator with an external drive. A drive having strength Ω and frequency ω_d is applied to the $|2\rangle \leftrightarrow |4\rangle$ transition [see Fig. 1(b)]. The Hamiltonian describing the system with the drive is given by

$$H = \sum_{i=1}^4 \omega_i |i\rangle\langle i| + \Omega(|2\rangle\langle 4|e^{i\omega_d t} + |4\rangle\langle 2|e^{-i\omega_d t}). \quad (6)$$

In the rotating frame of the drive described by the unitary transformation

$$\exp\{i[(\omega_d + \omega_2)|4\rangle\langle 4| + \omega_3|3\rangle\langle 3| + \omega_2|2\rangle\langle 2| + \omega_1|1\rangle\langle 1|]t\},$$

the total Hamiltonian becomes $H_R = \Delta|4\rangle\langle 4| + \Omega(|2\rangle\langle 4| + |4\rangle\langle 2|)$, where $\Delta = (\omega_4 - \omega_2) - \omega_d$. For the $|2\rangle \leftrightarrow |4\rangle$ drive considered here, the only surviving coherence under steady state is ρ_{42} (and its adjoint ρ_{24}). Therefore, dropping all other coherence terms and relabeling ϕ_2 as ϕ , the Q function defined in Eq. (1) can be expressed as

$$Q(\theta_1, \theta_2, \theta_3, \phi) = \text{Re}(\rho_{42}e^{i\phi})S_{\theta_1}S_{\theta_2}C_{\theta_3} + \rho_{11}S_{\theta_1}^2S_{\theta_2}^2S_{\theta_3}^2 + \rho_{22}S_{\theta_1}^2S_{\theta_2}^2C_{\theta_3}^2 + \rho_{33}S_{\theta_1}^2C_{\theta_2}^2 + \rho_{44}C_{\theta_1}^2. \quad (7)$$

Since the drive is not sensitively affecting the levels $|1\rangle$ and $|3\rangle$, without any loss of generality we can effectively set $\theta_2 = \pi$ and $\theta_3 = 0$ and replace θ_1 with θ in Eq. (7), which further simplifies the Husimi function to

$$Q(\theta, \phi) = \rho_{44}C_{\theta}^2 + \text{Re}(\rho_{42}e^{i\phi})S_{2\theta} + \rho_{22}S_{\theta}^2. \quad (8)$$

From this equation it is clear that nonzero ρ_{42} leads to the localization of the corresponding phase variable ϕ in the Husimi Q function. Such a state corresponds to the synchronized state. The synchronization measure $S(\phi_1, \phi_2, \phi_3)$ corresponding to Eq. (5) also reduces to

$$S(\phi) = \frac{\text{Re}(\rho_{42}e^{i\phi})}{16\pi^2}, \quad \max[S(\phi)] = \frac{|\rho_{42}|}{16\pi^2}, \quad (9)$$

which is nonzero only for $\rho_{42} \neq 0$, similar to [14].

III. NMR METHODOLOGY

A. Spin system and drive

In this work we consider a two-qubit system formed by the spin-1/2 nuclei ^{19}F and ^{31}P of sodium fluorophosphate molecule dissolved in D_2O solvent (5.3 mg of solute in 600 μl of solvent) and maintained at an ambient temperature of 298 K. All experiments were performed on a high-resolution Bruker 500-MHz NMR spectrometer operating at a magnetic field strength of $B_0 = 11.4$ T. Figure 1(a) displays the spin

system and its Hamiltonian parameters including scalar spin-spin coupling constant (J coupling), as well as the rf offsets ν_P and ν_F with respect to the Larmor frequencies $\omega_P = -\gamma_P B_0$ and $\omega_F = -\gamma_F B_0$, respectively, where γ_i are the gyromagnetic ratios. Note that ν_P is set to $-J/2$, while ν_F is set to zero. Figure 1(b) shows the Zeeman energy-level diagram of this two-qubit system. The laboratory-frame Hamiltonian is of the form

$$H_{\text{NMR}} = \omega_P I_z^P + \omega_F I_z^F + 2\pi J I_z^P I_z^F. \quad (10)$$

In NMR systems, at ambient temperatures, the thermal energy is much greater than the Zeeman energy splitting. Hence, an n -qubit system at thermal equilibrium is in a highly mixed state given by

$$\rho^{\text{eq}} = \exp\left(\frac{-H_0}{k_B T}\right) = \frac{\mathbb{1}}{2^n} + \sum_i \epsilon_i I_z^i, \quad (11)$$

where $\epsilon = \hbar\gamma_i B_0 / (2^n k_B T) \sim 10^{-5}$ is the purity factor. The population distribution in the high-temperature limit follows the Boltzmann distribution. The inherent relaxation (T_1) mechanism facilitates dissipation and helps establish an equilibrium population distribution, which forms a stable limit cycle with free phases as discussed in the preceding section. The thermal equilibrium spectra of ^{31}P and ^{19}F spins are shown in Figs. 1(c) and 1(d), respectively.

To realize synchronization, we apply a weak drive of amplitude $\Omega \approx 0.1$ Hz (explained in further detail in Sec. III C) selectively to the $|2\rangle \leftrightarrow |4\rangle$ transition as indicated in Fig. 1(b). The total Hamiltonian in the doubly rotating frame is given by

$$H_{\text{tot}} = H_0 + V \text{ where,}$$

$$H_0 = -2\pi\nu_P I_z^P + 2\pi J I_z^P I_z^F, \quad \text{and} \quad V = 2\pi\Omega I_y^P. \quad (12)$$

The first term with $\nu_P = -J/2$ makes the drive on-resonance with the $|2\rangle \leftrightarrow |4\rangle$ transition of the ^{31}P qubit that prepares ρ_{42} coherence [see Fig. 1(e)], while the dissipation mechanism redistributes the populations of the system.

B. Steady-state dynamics

We now describe a simple model to estimate the instantaneous state of the two-qubit system under different drive conditions. The time evolution of a quantum system is given by the master equation [43]

$$\frac{d\rho}{dt} = -i[H_0 + V, \rho] + \mathcal{D}[\hat{O}_+] \rho + \mathcal{D}[\hat{O}_-] \rho, \quad (13)$$

where H_0 is the internal Hamiltonian of the system and V represents the external drive. The thermal bath at a temperature T is modeled by the Lindblad superoperators $\mathcal{D}[\hat{O}_+] \rho + \mathcal{D}[\hat{O}_-] \rho$. The single quantum upward transitions [indicated by yellow curves in Fig. 1(b)] are described by the jump operator $\mathcal{D}[\hat{O}_+] \rho$ accompanied by their corresponding transition probabilities and rates. The equivalent downward transitions are described by the Hermitian conjugate $\mathcal{D}[\hat{O}_-] \rho$. The transition probabilities p_{ij}^{kl} can be identified with upward or downward transitions of a particular spin. We estimate these probabilities via the fermionic bath model [44]. Relabeling the upward and

downward transitions of the n th spin as $p_{n\pm}$, we may write

$$p_{n+} = \frac{1}{e^{4\epsilon_n} + 1}, \quad p_{n-} = 1 - p_{n+}, \quad (14)$$

which help maintain detailed balance. The transition rate of each spin is related to the bath temperature T via its spin-lattice relaxation time T_1^i as $g_i = 2\pi/T_1^i$ [see Fig. 1(a) for T_1 values]. The explicit forms of the Lindblad superoperators are given in Appendix B.

The master equation (13) is linear in ρ and can be written as

$$|\dot{\rho}\rangle = \mathcal{L}|\rho\rangle = (\mathcal{L}_0 + \mathcal{L}_V)|\rho\rangle, \quad (15)$$

where \mathcal{L} represents the Liouvillian superoperator describing the open system dynamics and $|\rho\rangle$ is the vectorized form of the density matrix in Liouville space. The mathematical form of \mathcal{L} can be obtained by applying the transformation $B\rho C \rightarrow C^* \otimes B|\rho\rangle$ to the master equation, where $|\rho\rangle$ is obtained by vertically stacking the columns of the density matrix [15,45–47].

The Liouvillian superoperator \mathcal{L} can be decomposed into two parts as shown in Eq. (15). The first part \mathcal{L}_0 defines the dynamics of the system in the absence of an external drive ($V = 0$) and is given by

$$\begin{aligned} \mathcal{L}_0 = & -i(I \otimes H_0 - H_0^* \otimes I) + \sum_{j=+,-} O_j^T \otimes O_j \\ & - \frac{1}{2}(I \otimes O_j^\dagger O_j + O_j^T O_j^* \otimes I). \end{aligned} \quad (16)$$

The second term \mathcal{L}_V represents the superoperator corresponding to an external perturbation V , which is given by

$$\mathcal{L}_V = -i(I \otimes V - V^* \otimes I). \quad (17)$$

The instantaneous state $\rho(t)$ after solving Eq. (15) is given by

$$\rho(t) = e^{\mathcal{L}t} \rho_0, \quad (18)$$

where ρ_0 represents the initial state of the system. The steady state is given by the converging solution of Eq. (15), defined as $\rho_{SS} = \lim_{t \rightarrow \infty} e^{\mathcal{L}t} \rho_0$. Therefore, the steady state corresponds to the eigenstate of the Liouvillian superoperator having zero eigenvalue [48]. In the absence of an external drive, one obtains a diagonal steady state $\rho^{\text{eq}} = \text{diag}\{\rho_{44}^{\text{eq}}, \rho_{33}^{\text{eq}}, \rho_{22}^{\text{eq}}, \rho_{11}^{\text{eq}}\}$, with elements following the thermal distribution. In the presence of an external drive V , the steady state corresponds to the eigenstate of \mathcal{L} having zero eigenvalue and is of the form

$$\rho^{\text{SS}} = \begin{bmatrix} \rho_{44}^{\text{SS}} & 0 & \rho_{42}^{\text{SS}} & 0 \\ 0 & \rho_{33}^{\text{SS}} & 0 & 0 \\ \rho_{24}^{\text{SS}} & 0 & \rho_{22}^{\text{SS}} & 0 \\ 0 & 0 & 0 & \rho_{11}^{\text{SS}} \end{bmatrix}. \quad (19)$$

Here the basis states are ordered according to decreasing energy eigenvalues. Also note that since the external drive is very weak, the steady state attained is close to the limit cycle, i.e., $\rho_{ii}^{\text{SS}} \approx \rho_{ii}^{\text{eq}}$.

We would like to emphasize that it is a highly nontrivial task to measure all the Lindblad dissipation operators for the NMR system [49]. The dynamics in the system is vastly more complex than the model considered here can capture. The

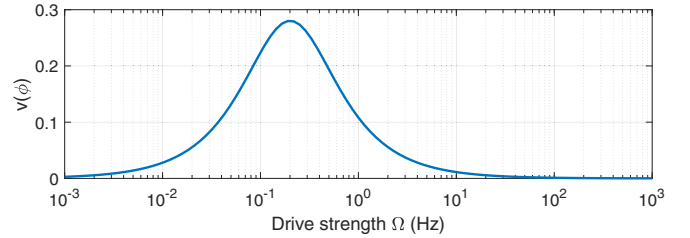


FIG. 2. Dependence of visibility of phase localization versus drive amplitude Ω , showing an optimum strength at around 0.1 Hz.

set of operators comprising this model is very minimal and intended only to capture the effective dissipation effects. We note that a full description of the NMR system involves many more terms not considered in our minimal model.

C. Optimum drive amplitude

The strength of the drive is crucial to realizing synchronization in any system. A very weak drive will barely perturb the system, while a very strong drive will induce forced behavior and alter the limit cycle. It is hence vital to limit the drive strength within an appropriate regime to achieve synchronization. For our system, we estimate the optimum drive strength using the numerical model described in Sec. III B. We vary the drive strength and numerically obtain the corresponding steady state, for which we estimate the visibility of the Husimi distribution

$$v(\phi) = \frac{\max(Q_\phi) - \min(Q_\phi)}{\max(Q_\phi) + \min(Q_\phi)}, \quad (20)$$

where $Q_\phi = \sum_\theta Q(\theta, \phi)$. Note that visibility quantifies the extent of phase localization. The result is shown in Fig. 2. The drive amplitude was varied from 10^{-3} Hz to 10^3 Hz. We can see that the visibility function is negligible for very low powers and then peaks at around 10^{-1} Hz before dropping to zero at higher drive amplitudes. We thus chose a drive strength of 0.1 Hz for our subsequent Husimi distribution experiments. The experimental method to calibrate the low-amplitude drive pulse is explained in Appendix C.

IV. INTERFEROMETRIC MEASUREMENT OF THE HUSIMI DISTRIBUTION

Theoretically, the instantaneous state can be directly predicted by solving the master equation, following which the Husimi function can be evaluated using Eq. (1). Experimentally, the standard way to extract the Husimi distribution is by using Eq. (1) after carrying out QST to estimate the steady-state density matrix ρ [37]. However, there are two unrelated issues that plague tomographic measurements in quantum systems. One relates to the fact that the experimental complexity of QST scales exponentially with the system size [50,51], each component of which has to be measured repeatedly. This introduces deleterious noise sources when multiple experiments are needed to perform QST. Nevertheless, for small quantum systems such as a four-level system, full tomography is routine. This leads us to the second issue, which is that even in the small system sizes considered here, QST of steady

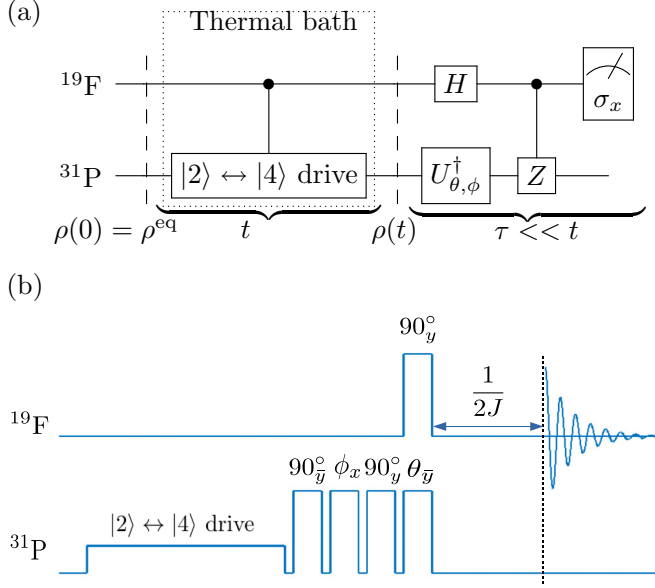


FIG. 3. (a) IMHD circuit for direct measurement of the Husimi distribution where the drive duration t is much longer than the measurement sequence time τ and (b) corresponding NMR pulse sequence.

states turns out to be highly inefficient. The reason is that QST relies on determining each element of the density matrix via a linear combination of expectation values of a set of observables. If the expectation values vary over large magnitudes, the dynamic range problem prevents the estimation of the faintest elements. The IMHD method described here avoids the dynamic range problem and directly extracts the Husimi function at each (θ, ϕ) value in a single experiment without requiring the elaborate QST protocols. This allows us to efficiently observe and quantify synchronization even after a very long drive, as explained below.

The circuit diagram representing the experiment to read the Husimi Q -function values is shown in Fig. 3(a). Here the ^{19}F qubit acts as the ancillary system, which along with the ^{31}P qubit begins from a thermal equilibrium state ρ^{eq} . The long weak drive responsible for synchronization is applied to the $|2\rangle \leftrightarrow |4\rangle$ transition of the ^{31}P qubit. As part of the interferometer, we now apply a Hadamard operator on ^{19}F qubit and prepare its superposition. Meanwhile, we apply the gate $U_{\theta, \phi}^\dagger$ on the ^{31}P qubit. Subsequently, we apply a controlled phase gate $\mathbb{1}_P \otimes |0\rangle\langle 0|_F + \sigma_z^P \otimes |1\rangle\langle 1|_F$.

Starting from the extremal state $|0, 0\rangle = |\theta = 0, \phi = 0\rangle$, we can generate the spin coherent state

$$|\theta, \phi\rangle = U_{\theta, \phi}|0, 0\rangle = [e^{-i\phi S_z} e^{-i\theta S_y} \otimes \mathbb{1}^F]|0, 0\rangle. \quad (21)$$

The corresponding IMHD reading is

$$\begin{aligned} Q_{\text{IF}}(\theta, \phi) &= \langle \theta, \phi | \rho^{\text{SS}} | \theta, \phi \rangle = \text{Tr}(\rho^{\text{SS}} |\theta, \phi\rangle \langle \theta, \phi|) \\ &= \text{Tr}(\rho^{\text{SS}} U_{\theta, \phi} |0, 0\rangle \langle 0, 0| U_{\theta, \phi}^\dagger) \\ &= \text{Tr}(U_{\theta, \phi}^\dagger \rho^{\text{SS}} U_{\theta, \phi} |0, 0\rangle \langle 0, 0|) \\ &= \langle |0, 0\rangle \langle 0, 0| \rho_{\theta, \phi}, \end{aligned} \quad (22)$$

where $\rho_{\theta, \phi} = U_{\theta, \phi}^\dagger \rho^{\text{SS}} U_{\theta, \phi}$.

The NMR pulse sequence for the IMHD is shown in Fig. 3(b). After the $|2\rangle \leftrightarrow |4\rangle$ drive, we implement a pseudo-Hadamard operator using a 90_y° pulse on the ^{19}F spin. While $U_\theta^\dagger = e^{i\theta I_y}$ can be realized by a single θ_y pulse, $U_\phi^\dagger = e^{i\phi I_z} = e^{-i(\pi/2)I_y} e^{-i\phi I_x} e^{i(\pi/2)I_y}$ is realized by a sequence of three pulses. The measurement of the $|0, 0\rangle\langle 0, 0|$ projector can be realized via a controlled phase gate, which can be implemented, up to a phase factor, by a simple free evolution under the system Hamiltonian $2\pi J I_z^P I_z^F$ for a time duration of $1/2J$. A subsequent measurement of transverse magnetization of the ^{19}F spin yields the NMR signal

$$s = \text{Re}\langle \sigma_x^F \rangle = \frac{1}{2} \{ C_{2\theta} [\rho_{11}^{\text{SS}} - \rho_{22}^{\text{SS}} - \rho_{33}^{\text{SS}} + \rho_{44}^{\text{SS}}] + S_{2\theta} \text{Re}(e^{-i\phi} \rho_{24}^{\text{SS}} + e^{i\phi} \rho_{42}^{\text{SS}}) \}. \quad (23)$$

One can verify from Eqs. (7) and (23) that

$$Q_{\text{IF}}(\theta, \phi) = \frac{24}{\pi^3} \left[\frac{1+2s}{2} - (\rho_{11}^{\text{SS}} C_\theta^2 + \rho_{33}^{\text{SS}} S_\theta^2) \right] = Q(\theta, \phi). \quad (24)$$

Here $\rho_{11}^{\text{SS}} \simeq \rho_{11}^{\text{eq}}$ and $\rho_{33}^{\text{SS}} \simeq \rho_{33}^{\text{eq}}$ are the populations of undriven levels and can be estimated from the thermal equilibrium population distribution. For the highly mixed NMR systems, $\rho_{11} \simeq \rho_{33} \simeq 1/4$, so

$$Q_{\text{IF}}(\theta, \phi) = \frac{24}{\pi^3} \left[\frac{1+2s}{2} - \frac{1}{4} \right] = \frac{24}{\pi^3} \left[s + \frac{1}{4} \right]. \quad (25)$$

Thus, the ^{19}F signal after the IMHD circuit of Fig. 3 can directly measure the Husimi distribution values. One such spectrum for a particular drive duration and (θ, ϕ) values is shown in Fig. 1(f). Note that one may use a third spin as an ancilla qubit for the interferometer circuit, but it will open up additional dissipation pathways. To minimize such decoherence channels, we have used one of the system spins itself as an ancilla qubit.

V. RESULTS

The experimental IMHD results at thermal equilibrium as well as at various drive durations are shown in Fig. 4. The signal measured at the end of the IMHD circuit (Fig. 3) is directly used to estimate the Husimi distributions using Eq. (25). Indicated above each panel is the value of the corresponding visibility factor of the Husimi distribution.

Limit cycle. In the absence of drive, the system is in thermal equilibrium with the environment. Husimi distribution of the thermal equilibrium state ρ^{eq} is shown in Fig. 4(a), which is uniform throughout the phase space with no phase localization and an accordingly vanishingly small visibility factor. Therefore, ρ^{eq} is a valid limit cycle with free phase, as is expected.

Onset of synchronization. To study synchronization in the system, we apply a weak transition-selective drive of strength $\Omega = 0.1$ Hz on-resonant with the $|2\rangle \leftrightarrow |4\rangle$ transition as shown in Fig. 1(b). The equilibration time of the quantum system is approximately 10 s, which means that the dynamics captured under 10 s can be considered transient whereas for timescales much larger than 10 s we observe steady states of the system. The drive is applied for different durations, which enables us to investigate the transient and steady-state

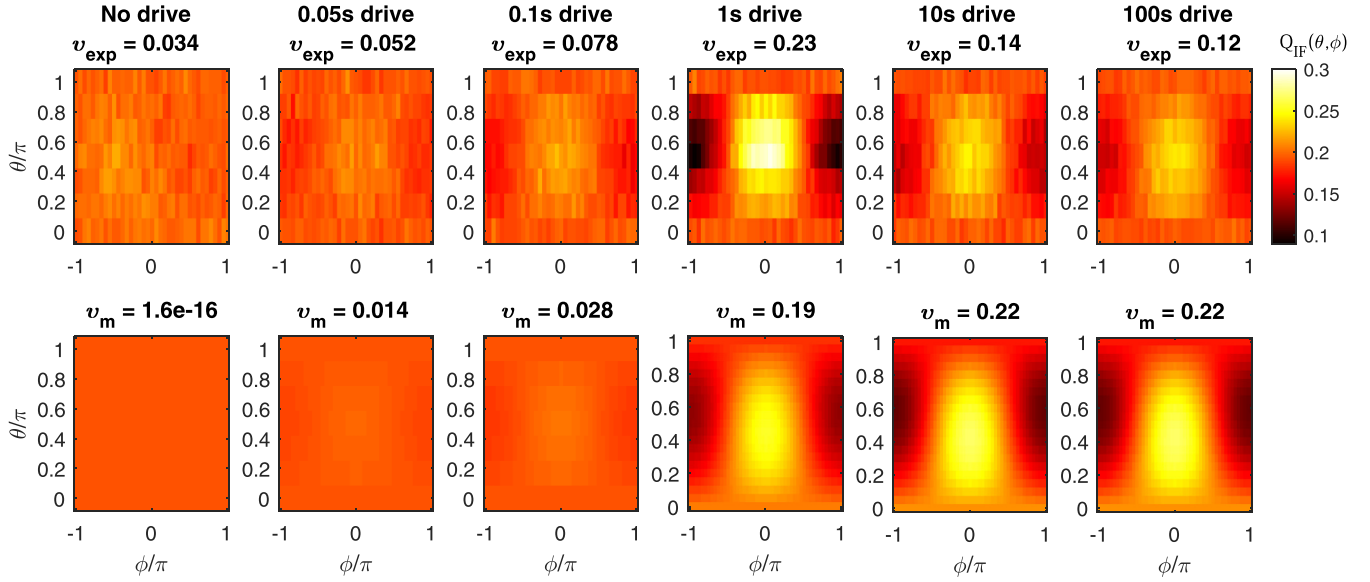


FIG. 4. Full phase-space Husimi distribution values for different drive durations to capture transient and steady-state behavior in the subspace of interest obtained by (a) experiments and (b) the numerical model. The values above each panel indicate the visibility factors of the Husimi distributions. We can see that in the absence of a drive, there is no localization in the phase space. Upon applying the drive, in the transient regime (up to 10 s), the phase begins to localize gradually, showing the strongest localization experimentally at a drive duration of 1 s and saturating after 10 s.

dynamics in the subspace of interest. The experimentally measured Husimi distributions for various drive durations are shown in Fig. 4(a). The corresponding distributions for the instantaneous states predicted by the numerical model (described in Sec. III B) are shown in Fig. 4(b). We can see that the system gradually develops phase localization with the drive before reaching a steady state. For short drive durations, i.e., for 50 and 100 ms, we observe a weak phase localization, which captures the transient dynamics. In this transient regime, the experimental phase distribution reaches a peak localization strength at 1 s drive duration. The system then reaches a steady state with the phase localization stabilizing for drive durations roughly above 10 s. It remains synchronized even up until 100 s, which is more than ten times the drive period as well as ten times the T_1 relaxation time constants of the system spins.

The experimental phase localization pattern and visibility factors match fairly well with those predicted by the numerical model. While an elaborate relaxation model, accounting for all the Lindblad dissipation operators and other experimental imperfections such as rf inhomogeneity might explain the observed deviations, the current minimal model nonetheless captures the essential signatures of synchronization.

Arnold tongue. The Arnold tongue is a quintessential test of synchronization that probes robustness of phase localization against small changes in drive strengths and drive detuning [1]. As the drive strength is increased, the region of synchronization can be shown to be wider, leading to the familiar tongue shape. Here we vary the drive strength of the 100 s weak drive and its resonance offset by 3 Hz about the resonance value. The Arnold tongue is quantified using the maximum of the synchronization measure $\max[S(\phi)]$ and in the present case it is only dependent on the ρ_{42} element of the density matrix, as evident from Eq. (9). Experimentally,

this can be directly measured from the intensity of the ^{31}P NMR spectrum [see Fig. 1(e)]. Figure 5 compares the result of the Arnold tongue experiments with that of the numerical prediction (from the model described in Sec. III B). For strong drive strength and near-resonance conditions, the degree of synchronization is higher since the drive has a more efficient perturbative effect on the system. On the other hand, for larger detuning and weaker drives, the extent of synchronization is weaker. The experimental data show pixelation since the drive strength is varied in a discrete fashion. Moreover, in the limit of vanishing drive strength, we expect no synchronization, which could not be captured experimentally since the rf pulse calibration is reliable only until a certain lower threshold, as elaborated in Appendix C. Despite an overall correspondence between the experimental and the predicted profiles, we see a higher spread along the detuning axis in the experimental

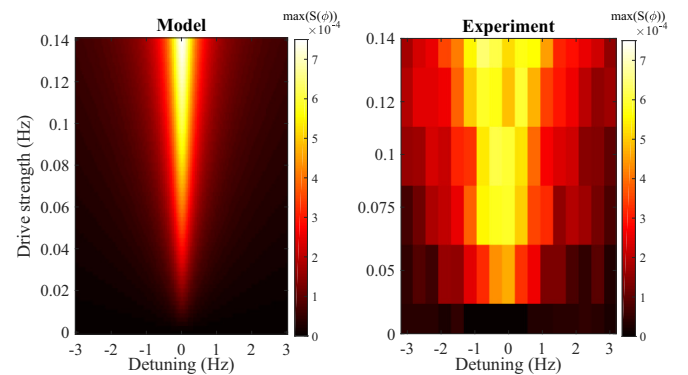


FIG. 5. Arnold tongue behavior of the system. The system shows strongest synchronization for on-resonant drive and strong drive strengths, while off-resonant drives are unable to synchronize with the transition of interest even for large driving strengths.

data, which can be attributed to the limitations of the minimal numerical model and experimental imperfections.

VI. SUMMARY AND OUTLOOK

Recently, there has been an increasing interest in studying the synchronization of quantum systems with external drives under suitable conditions. In this work we experimentally demonstrated synchronization in a two-qubit system using NMR architecture. We used the Husimi distribution function as a witness for synchronization. We applied a weak transition-selective drive on one of the spins and observed the gradual onset of phase localization via the Husimi distribution. In the absence of any external drive, the system evolves under its internal Hamiltonian as well as inherent relaxation mechanisms, thereby settling to its thermal equilibrium state. The corresponding Husimi distribution pattern has no phase preference, and hence the thermal equilibrium state forms the valid limit cycle of the system.

An interesting issue that arises with the study of the steady-state dynamics of open quantum systems relates to the fact that NMR signals are proportional to the population differences. Since the populations are in a pseudospin state, their effective difference dips below the noise threshold, rendering steady-state population tomography difficult in such systems until now. Here we reported an interferometric technique to directly extract the Husimi distribution values by reading the signal of the undriven spin. The interferometric method is significantly more efficient compared to the standard method based on quantum state tomography.

To establish the robustness of synchronization, we investigated the response of the system to changes in drive strengths and drive detuning. The resulting phase-localization measure of the system exhibited the expected Arnold tongue behavior. We compared the experimental results with a minimalistic T_1 relaxation model of the two-qubit nuclear-spin system, which could capture the general features of the experimental data.

This work demonstrates the suitability of NMR architecture for quantum synchronization studies and also opens up avenues for further exploration of the phenomenon in larger spin systems as well as under a variety of interactions and drive conditions. One can envisage NMR systems being useful for studying the implications of synchronization in areas such as spectroscopy, quantum computing, and quantum thermodynamics.

ACKNOWLEDGMENTS

V.R.K. acknowledges valuable discussions with Conan Alexander. S.V. acknowledges support from a Government of India DST-SERB Early Career Research Award (Grant No. ECR/2018/000957) and DST-QUEST Grant No. DST/ICPS/QuST/Theme-4/2019. T.S.M. acknowledges funding from Grant No. DST/ICPS/QuST/2019/Q67.

APPENDIX A: SPIN COHERENT STATES

Spin coherent states are routinely used to study synchronization since their evolutions are closest to classical trajectories [52]. Furthermore, coherent states exhibit stable

oscillations as explained below. For a spin-1/2 particle, the z projection of the spin angular momentum S_z is quantized into $2s + 1$ levels $|S, m_s\rangle$ with eigenvalues $m_s = -1/2, 1/2$. The spin coherent state for this spin in the SU(2) group can be described as a rotation of the extremal state $|S, S\rangle$ such that [41,53,54]

$$|\hat{n}_2\rangle = |\theta, \phi\rangle = e^{-i\phi S_z} e^{-i\theta S_y} |S, S\rangle = \begin{pmatrix} C_\theta \\ e^{i\phi} S_{\theta_1} \end{pmatrix}, \quad (\text{A1})$$

where $\theta \in [0, \pi]$, $\phi \in [0, 2\pi]$, $C_\theta = \cos(\theta/2)$, and $S_\theta = \sin(\theta/2)$. It is obvious that spin-1/2 coherent states can be mapped to points on the surface of the Bloch sphere. The recursive construction of spin coherent state vectors for an n -level nondegenerate system is [40,41]

$$|\hat{n}_n\rangle = \begin{pmatrix} C_\theta \\ 0 \\ \vdots \\ 0 \end{pmatrix} + e^{i\phi} S_\theta \begin{pmatrix} 0 \\ |\hat{n}_{n-1}\rangle \end{pmatrix}. \quad (\text{A2})$$

Note that each lower-level vector $|\hat{n}_{n-1}\rangle$ is made up of a new pair of angular variables. From the above, we obtain the SU(4) coherent states in the form

$$|\hat{n}_4\rangle = \begin{pmatrix} C_{\theta_1} \\ e^{i\phi_1} S_{\theta_1} C_{\theta_2} \\ e^{i\phi_2} S_{\theta_1} S_{\theta_2} C_{\theta_3} \\ e^{i\phi_3} S_{\theta_1} S_{\theta_2} S_{\theta_3} \end{pmatrix}. \quad (\text{A3})$$

From the above definition, we can see that populations are governed by the parameters $(\theta_1, \theta_2, \theta_3)$ and phases by the parameters (ϕ_1, ϕ_2, ϕ_3) .

APPENDIX B: LINDBLAD RELAXATION OPERATORS

The explicit form of the single-quantum jump operators considered for the four-level system shown in Fig. 1(b) are explained here. The single-quantum transition of the first qubit implies that the system in a state $|i\rangle|j\rangle$ goes to the state $|k\rangle|l\rangle$, where $k = i \pm 1$ and $l = j$. The same can be extended to the single-quantum transition of the second qubit. The Lindblad superoperator for upward transitions of the combined two-qubit system is hence given by $\mathcal{D}[\hat{O}_+] \rho = \sum_{(k=i-1, l=j)} \mathcal{D}[\mathcal{O}_{ij}^{kl}] \rho + \sum_{(k=i, l=j-1)} \mathcal{D}[\mathcal{O}_{ij}^{kl}] \rho$, where $\mathcal{D}[\hat{O}] \rho = \hat{O} \rho \hat{O}^\dagger - \{\hat{O}^\dagger \hat{O}, \rho\}/2$ and the jump operator \mathcal{O}_{ij}^{kl} is defined as $\mathcal{O}_{ij}^{kl} = \sqrt{g_{ij}^{kl} p_{ij}^{kl}} |k\rangle|l\rangle \langle i| \langle j|$. Similarly, we can write $\mathcal{D}[\hat{O}_-] \rho = \sum_{(k=i+1, l=j)} \mathcal{D}[\mathcal{O}_{ij}^{kl}] \rho + \sum_{(k=i, l=j+1)} \mathcal{D}[\mathcal{O}_{ij}^{kl}] \rho$, where $\mathcal{O}_{ij}^{kl} = (\mathcal{O}_{ij}^{kl})^\dagger$. The coefficients of the jump operators corresponding to each qubit determine the transition rate given by g_{ij}^{kl} and the transition probability given by p_{ij}^{kl} . The transition rate is dependent on the bath temperature via the spin-lattice relaxation time constant T_1 , and the transition probabilities are derived from a fermionic bath model, as explained in the main text.

APPENDIX C: VERY-LOW-POWER RF CALIBRATION

As discussed in Sec. III C, observation of phase synchronization requires a drive of amplitude 10^{-1} Hz. The

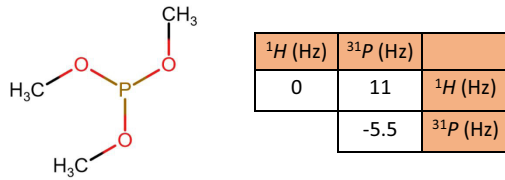


FIG. 6. TMP molecule and Hamiltonian parameters.

calibration of such very weak radio frequency is nontrivial, since the signal-to-noise ratio is negligibly small. For this purpose, we used another spin system trimethylphosphite dissolved in dimethylsulphoxide solvent. We specifically chose this sample because of its star topology with ^{31}P at the center coupled to nine identical ^1H nuclei with a scalar J coupling constant of 11 Hz, as shown in Fig. 6. Such geometry is highly preferable since the magnetization of the nine high γ proton nuclei can be easily transferred to the central ^{31}P nucleus via insensitive nuclei enhanced by the polarization transfer (INEPT) and further algorithmic cooling, thus boosting its signal [55]. This gives a better signal-to-noise ratio and hence more accurate calibration values. For very low amplitudes, the signal is proportional to $\sin(\Omega t) \approx \Omega t$ and therefore we expect a linear dependence. The calibration results are shown in Fig. 7. As we can see, the intensity of the ^{31}P spectrum after decoupling protons varies linearly with time for the low-amplitude pulses. Thus, by fitting a linear function to the resulting curve, we can backcalculate the exact amplitude of

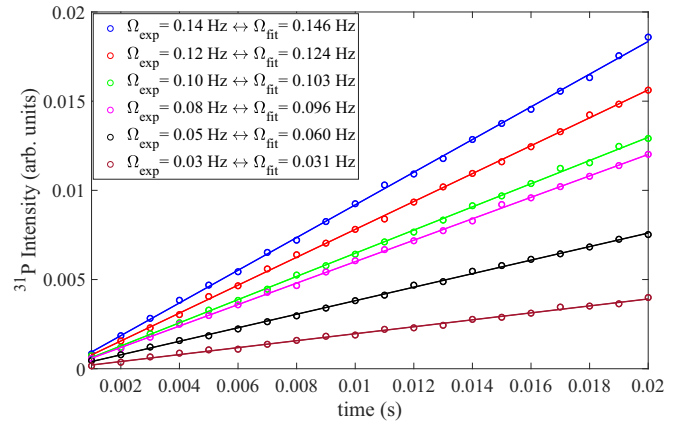


FIG. 7. Low-power calibration using trimethylphosphite. The intensity of the ^{31}P spin after decoupling protons is shown as a function of time for various low-amplitude pulses. We can see that the response is linear in this regime. The expected and exactly obtained values from backcalculation of the linear fit are shown in the legend.

the pulse. The estimated and exact values from backcalculation of the linear fit are shown in the legend. Radio-frequency fields with amplitudes lower than 0.03 Hz could not be calibrated as the power corresponding to such pulses was below the threshold of the hardware. These low-power pulses were used in the Husimi distribution estimation and Arnold tongue experiments.

- [1] A. Pikovsky, J. Kurths, M. Rosenblum, and J. Kurths, *Synchronization: A Universal Concept in Nonlinear Sciences* (Cambridge University Press, Cambridge, 2003).
- [2] T. E. Lee and H. R. Sadeghpour, Quantum Synchronization of Quantum van der Pol Oscillators with Trapped Ions, *Phys. Rev. Lett.* **111**, 234101 (2013).
- [3] M. R. Hush, W. Li, S. Genway, I. Lesanovsky, and A. D. Armour, Spin correlations as a probe of quantum synchronization in trapped-ion phonon lasers, *Phys. Rev. A* **91**, 061401(R) (2015).
- [4] S. E. Nigg, Observing quantum synchronization blockade in circuit quantum electrodynamics, *Phys. Rev. A* **97**, 013811 (2018).
- [5] M. Xu, D. A. Tieri, E. C. Fine, J. K. Thompson, and M. J. Holland, Synchronization of Two Ensembles of Atoms, *Phys. Rev. Lett.* **113**, 154101 (2014).
- [6] M. Ludwig and F. Marquardt, Quantum Many-Body Dynamics in Optomechanical Arrays, *Phys. Rev. Lett.* **111**, 073603 (2013).
- [7] S. Walter, A. Nunnenkamp, and C. Bruder, Quantum Synchronization of a Driven Self-Sustained Oscillator, *Phys. Rev. Lett.* **112**, 094102 (2014).
- [8] S. Walter, A. Nunnenkamp, and C. Bruder, Quantum synchronization of two van der Pol oscillators, *Ann. Phys. (Berlin)* **527**, 131 (2015).
- [9] W. Li, C. Li, and H. Song, Quantum synchronization in an optomechanical system based on Lyapunov control, *Phys. Rev. E* **93**, 062221 (2016).
- [10] M. Zhang, G. S. Wiederhecker, S. Manipatruni, A. Barnard, P. McEuen, and M. Lipson, Synchronization of Micromechanical Oscillators Using Light, *Phys. Rev. Lett.* **109**, 233906 (2012).
- [11] C. A. Holmes, C. P. Meaney, and G. J. Milburn, Synchronization of many nanomechanical resonators coupled via a common cavity field, *Phys. Rev. E* **85**, 066203 (2012).
- [12] D. Withaut, S. Wimberger, R. Burioni, and M. Timme, Classical synchronization indicates persistent entanglement in isolated quantum systems, *Nat. Commun.* **8**, 14829 (2017).
- [13] A. Roulet and C. Bruder, Quantum Synchronization and Entanglement Generation, *Phys. Rev. Lett.* **121**, 063601 (2018).
- [14] N. Jaseem, M. Hajdušek, V. Vedral, R. Fazio, L.-C. Kwek, and S. Vinjanampathy, Quantum synchronization in nanoscale heat engines, *Phys. Rev. E* **101**, 020201(R) (2020).
- [15] P. Solanki, N. Jaseem, M. Hajdušek, and S. Vinjanampathy, Role of coherence and degeneracies in quantum synchronization, *Phys. Rev. A* **105**, L020401 (2022).
- [16] W. Li, C. Li, and H. Song, Quantum synchronization and quantum state sharing in an irregular complex network, *Phys. Rev. E* **95**, 022204 (2017).
- [17] M. Hajdušek, P. Solanki, R. Fazio, and S. Vinjanampathy, Seeding Crystallization in Time, *Phys. Rev. Lett.* **128**, 080603 (2022).
- [18] A. Roulet and C. Bruder, Synchronizing the Smallest Possible System, *Phys. Rev. Lett.* **121**, 053601 (2018).
- [19] N. Jaseem, M. Hajdušek, P. Solanki, L.-C. Kwek, R. Fazio, and S. Vinjanampathy, Generalized measure of quantum synchronization, *Phys. Rev. Research* **2**, 043287 (2020).

- [20] W. P. Schleich, *Quantum Optics in Phase Space* (Wiley, New York, 2011).
- [21] F. Galve, G. Luca Giorgi, and R. Zambrini, in *Lectures on General Quantum Correlations and their Applications*, edited by F. Franchini, D. Soares Pinto, and G. Adesso, Quantum Science and Technology (Springer International Publishing, Cham, 2017), pp. 393–420.
- [22] W. Li, W. Zhang, C. Li, and H. Song, Properties and relative measure for quantifying quantum synchronization, *Phys. Rev. E* **96**, 012211 (2017).
- [23] M. Koppenhöfer and A. Roulet, Optimal synchronization deep in the quantum regime: Resource and fundamental limit, *Phys. Rev. A* **99**, 043804 (2019).
- [24] A. Mari, A. Farace, N. Didier, V. Giovannetti, and R. Fazio, Measures of Quantum Synchronization in Continuous Variable Systems, *Phys. Rev. Lett.* **111**, 103605 (2013).
- [25] G. Manzano, F. Galve, G. L. Giorgi, E. Hernández-García, and R. Zambrini, Synchronization, quantum correlations and entanglement in oscillator networks, *Sci. Rep.* **3**, 1439 (2013).
- [26] V. Ameri, M. Eghbali-Arani, A. Mari, A. Farace, F. Kheirandish, V. Giovannetti, and R. Fazio, Mutual information as an order parameter for quantum synchronization, *Phys. Rev. A* **91**, 012301 (2015).
- [27] S. Sonar, M. Hajdušek, M. Mukherjee, R. Fazio, V. Vedral, S. Vinjanampathy, and L.-C. Kwek, Squeezing Enhances Quantum Synchronization, *Phys. Rev. Lett.* **120**, 163601 (2018).
- [28] B. Buca, C. Booker, and D. Jaksch, Algebraic theory of quantum synchronization and limit cycles under dissipation, *SciPost Phys.* **12**, 097 (2022).
- [29] G. Karpat, I. Yalçinkaya, B. Çakmak, G. L. Giorgi, and R. Zambrini, Synchronization and non-Markovianity in open quantum systems, *Phys. Rev. A* **103**, 062217 (2021).
- [30] G. Karpat, I. Yalçinkaya, and B. Çakmak, Quantum synchronization of few-body systems under collective dissipation, *Phys. Rev. A* **101**, 042121 (2020).
- [31] G. Karpat, I. Yalçinkaya, and B. Çakmak, Quantum synchronization in a collision model, *Phys. Rev. A* **100**, 012133 (2019).
- [32] G. L. Giorgi, F. Galve, and R. Zambrini, Probing the spectral density of a dissipative qubit via quantum synchronization, *Phys. Rev. A* **94**, 052121 (2016).
- [33] G. L. Giorgi, F. Plastina, G. Francica, and R. Zambrini, Spontaneous synchronization and quantum correlation dynamics of open spin systems, *Phys. Rev. A* **88**, 042115 (2013).
- [34] M. Koppenhöfer, C. Bruder, and A. Roulet, Quantum synchronization on the IBM Q system, *Phys. Rev. Research* **2**, 023026 (2020).
- [35] A. W. Laskar, P. Adhikary, S. Mondal, P. Katiyar, S. Vinjanampathy, and S. Ghosh, Observation of Quantum Phase Synchronization in Spin-1 Atoms, *Phys. Rev. Lett.* **125**, 013601 (2020).
- [36] I. Bengtsson and K. Życzkowski, *Geometry of Quantum States: An Introduction to Quantum Entanglement* (Cambridge University Press, Cambridge, 2006).
- [37] V. R. Krithika, V. S. Anjusha, U. T. Bhosale, and T. S. Mahesh, NMR studies of quantum chaos in a two-qubit kicked top, *Phys. Rev. E* **99**, 032219 (2019).
- [38] K. Husimi, Some formal properties of the density matrix, *Proc. Phys.-Math. Soc. Jpn.* **22**, 264 (1940).
- [39] Y. Kano, A new phase-space distribution function in the statistical theory of the electromagnetic field, *J. Math. Phys.* **6**, 1913 (1965).
- [40] A. Perelomov, *Generalized Coherent States and Their Applications* (Springer, Berlin, 1986).
- [41] K. Nemoto, Generalized coherent states for $SU(n)$ systems, *J. Phys. A: Math. Gen.* **33**, 3493 (2000).
- [42] M. Mathur and H. Mani, $SU(N)$ coherent states, *J. Math. Phys.* **43**, 5351 (2002).
- [43] H.-P. Breuer and F. Petruccione, *The Theory of Open Quantum Systems* (Oxford University Press on Demand, 2002).
- [44] A. Ghosh, S. S. Sinha, and D. S. Ray, Fermionic oscillator in a fermionic bath, *Phys. Rev. E* **86**, 011138 (2012).
- [45] N. Suri, F. C. Binder, B. Muralidharan, and S. Vinjanampathy, Speeding up thermalisation via open quantum system variational optimisation, *Eur. Phys. J.: Spec. Top.* **227**, 203 (2018).
- [46] D. Manzano, A short introduction to the Lindblad master equation, *AIP Adv.* **10**, 025106 (2020).
- [47] J. A. Gyamfi, Fundamentals of quantum mechanics in Liouville space, *Eur. J. Phys.* **41**, 063002 (2020).
- [48] C. Navarrete-Benlloch, Open systems dynamics: Simulating master equations in the computer, [arXiv:1504.05266](https://arxiv.org/abs/1504.05266).
- [49] N. Boulant, T. F. Havel, M. A. Pravia, and D. G. Cory, Robust method for estimating the Lindblad operators of a dissipative quantum process from measurements of the density operator at multiple time points, *Phys. Rev. A* **67**, 042322 (2003).
- [50] I. L. Chuang, N. Gershenfeld, M. G. Kubinec, and D. W. Leung, Bulk quantum computation with nuclear magnetic resonance: Theory and experiment, *Proc. R. Soc. A* **454**, 447 (1998).
- [51] A. Shukla, K. R. K. Rao, and T. S. Mahesh, Ancilla-assisted quantum state tomography in multiqubit registers, *Phys. Rev. A* **87**, 062317 (2013).
- [52] Y. L. Loh and M. Kim, Visualizing spin states using the spin coherent state representation, *Am. J. Phys.* **83**, 30 (2015).
- [53] J. Radcliffe, Some properties of spin coherent states, *J. Phys. A: Math. Gen* **4**, 313 (1971).
- [54] J. R. Klauder and B. Skagerstam, *Coherent States: Applications in Physics and Mathematical Physics* (World Scientific, Singapore, 1985).
- [55] V. R. Pande, G. Bhole, D. Khurana, and T. S. Mahesh, Strong algorithmic cooling in large star-topology quantum registers, *Phys. Rev. A* **96**, 012330 (2017).